NANO LETTERS

pubs.acs.org/NanoLett

Gold Mesostructures with Tailored Surface Topography and Their Self-Assembly Arrays for Surface-Enhanced Raman Spectroscopy

Jixiang Fang,*,†,§ Shuya Du,† Sergei Lebedkin,§ Zhiyuan Li,† Robert Kruk,§ Manfred Kappes,§ and Horst Hahn§

†MOE Key Laboratory for Nonequilibrium Synthesis and Modulation of Condensed Matter, School of Science, Xi'an Jiaotong University, Shann Xi, 710049, People's Republic of China, †Institute of Physics, Chinese Academy of Sciences, Beijing, 100080, People's Republic of China, and §Karlsruhe Institut für Technologie (KIT), Institut für Nanotechnologie, Karlsruhe 76021, Germany

ABSTRACT We report a facile particle mediated aggregation protocol to synthesize "sea urchin"-like gold mesoparticles with tailored surface topography via a secondary nucleation and growth process. Surprisingly, these multitip Au mesoparticles are capable of self-assembling into monolayer or multiple layer arrays on Si substrates with a convincing reproducibility and homogeneity over large areas. Raman measurements show that these individual sea urchin-like multitipped gold mesoparticles exhibit a high enhancement of surface-enhanced Raman scattering (SERS). In addition, the sea urchin-like mesoparticle arrays display a further enhancement of SERS by 1 or 2 orders of magnitude over the individual mesoparticle due to the formation of additional hot spots between the particles. The current protocol stands out as a potentially interesting approach for the fabrication of technologically important SERS-based sensors.

KEYWORDS Gold mesostructures, sea urchin-like, surface topography, self-assembly, SERS

Surface-enhanced Raman scattering (SERS) spectroscopy has been intensely explored as a powerful and extremely sensitive analytical technique with applications in biochemistry, chemical production, and environmental monitoring.[1−4] So far, three main classes of SERS substrates have been developed: metallic rough surfaces, nanoparticle colloids, and periodic nanostructures. Although the SERS effect with a giant enhancement factor (EF) of up to $\sim 10^{12}-10^{13}$ has been demonstrated for analyte molecules located at so-called "hot spots", the fabrication of SERS substrates with a stable, uniform, and high average EF over relatively large areas remains a great challenge.[1] Currently, the reproducibility and homogeneity can be realized through the use of advanced top-down nanopatterning techniques such as electron beam lithography; however these techniques are associated with limitations regarding throughput, cost, and processable materials. Moreover, it is still difficult to fabricate well-controlled small gaps or complex geometries on the scale of a few nanometers to create efficient and abundant "hot spots". As a result, only a moderate enhancement (EF $\sim 10^5-10^6$) has typically been achieved for lithographically produced substrates[2,3] such as commercially available Klarite.[4]

The SERS effect is highly dependent upon the nanoparticle size and shape as it relates to the excitation wavelength and the dielectric properties of the medium. For small nanoparticles, e.g., ~50 nm, only a dipolar plasmon mode can be excited. As the particle size is increased above 50 nm, higher-order multipolar plasmonic modes appear and scattering effects become more significant, thus the plasmon band gets noticeably red-shifted and broadened. When particle sizes above 100 nm are reached, dephasing starts to occur and new plasmon modes can be accommodated within the particle. These effects are important for applications such as photonics, photocatalysis, and SERS. To date, higher order multipole resonances have been reported for larger particles and metallic nanoshells with sizes above 200 nm.[5,6] SERS measurements for films of Au nanoparticles also show that Au nanoparticles with a larger particle size (>170 nm) are capable of self-organizing into planar close-packed arrays and thus can display a uniform SERS activity.[7] In fact, "hot spots" in assemblies (arrays) of small particles result in mode coupling and are usually found in tiny gaps between neighboring particles. Hence the ratio of the gap over the particle size is a critical parameter for EF.[8] In this regard, assemblies of small compact particles may not be the best approach to create "bright" "hot spots" within a certain area.

In addition to the metallic nature and size or shape, the surface topography of the particles can also be a significant factor to tailor the optical properties. Up to now, only a few recent studies have explored the relationship between surface roughness and optical properties. For instance, theoretical and experimental investigations indicated that nanoscale

* To whom correspondence should be addressed, jxfang@mail.xjtu.edu.cn.
Received for review: 09/7/2010
Published on Web: 11/19/2010

DOI: 10.1021/nl103161q | *Nano Lett.* **2010,** *10,* 5006–5013

surface texture can introduce dramatic changes to the plasmonic response of Au nanoshells, where quadrupole damping takes place.[9] Even surface roughness of only a few atomic layers can also generate red shifts in longitudinal surface plasmon modes.[10,11] As a result, the SERS properties of Au or Ag mesoscopic nanoparticles with irregular nanoscale roughness and deeply creviced surface morphology have been attracting increasing interest.[12−14] For example, Halas and co-workers synthesized Au "meatball-like" particles with randomly arranged irregular nanoscale protrusions through an organic reduction route using gum Arabic as the stabilizer.[13] Xu and co-workers prepared highly surface-roughened "flower-like" Ag nanoparticles by means of poly(vinyl pyrrolidone) (PVP) surfactant in an aqueous environment.[14] With a spherical shape and roughened morphology, SERS EFs more than 10^7 were obtained with a relatively good reproducibility. Note that some complex morphologies, such as Pt "sea urchins"[15,16] and nanodendrites,[17] Au nanostars,[18] multipods,[19] and branched nanocrystals,[20] Ni "sea urchin"-like particles,[21] have been reported previously. However, a unique surface morphology with a huge amount of multiple tips (e.g., hundreds) remains quite rare, particularly in Au and Ag. Furthermore, although it has been recognized that the optical properties of nanoparticles depend not only on their size and shape but also on their surface topography, no effective approaches have been exploited so far to systematically modify the surface topography and thereby the properties of metallic nanoparticles in a controlled manner.

Mesocrystals are a 3D crystallographically ordered superstructure of nanoparticles formed via a particle-mediated growth mechanism, involving the crystallographically ordered aggregation of individual nanoparticle subunits.[22] It is interesting to note that for many systems the particle-mediated aggregation can yield mesocrystals, i.e., 3D mesostructures with well-oriented subunits. These include, for instance, Ag_2O,[23] Cu_2O,[24] ZnO,[25] as well as Au[26] and Ag.[27,28] The resulting mesocrystals are characterized by a rough surface, small building blocks (around tens of nanometers scale), and notable internal porosity. Mesoparticles with such features are interesting not only for SERS, but also for other applications such as catalysis, photonics, and sensors.[23] In this paper, we report a particle-mediated growth protocol to synthesize "sea urchin"-like Au mesoparticles by using a secondary nucleation process. These sea urchin-like mesoparticles with tailored surface topography possess unique structural features that exhibit high SERS activity, making them very attractive as Raman sensors. Importantly, these sea urchin-like mesoparticles can spread and self-assemble to form monolayer or multiple layer arrays, and demonstrate highly reproducible and homogeneous SERS effects over a large area. Thus they are promising candidates for SERS sensor substrates-combining high performance with simple preparation and low cost.

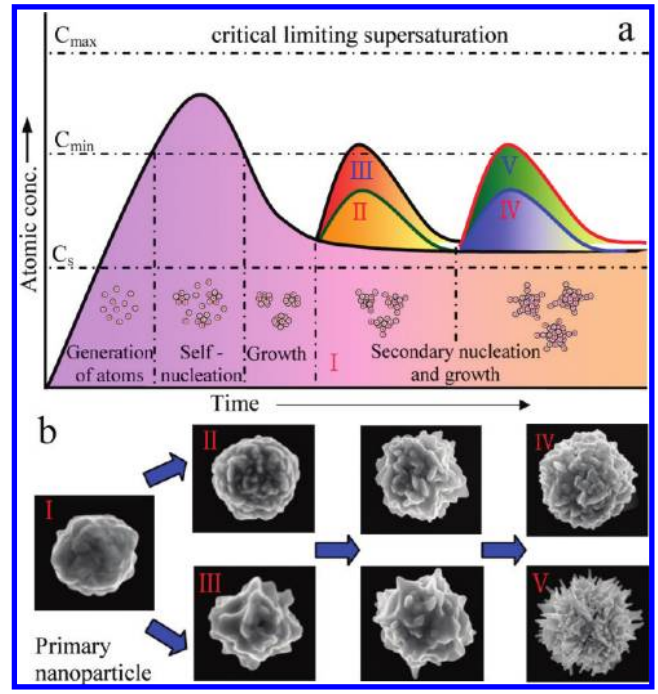

FIGURE 1. (a) Schematic plot of a gold atom concentration versus time illustrating the growth of mesoparticles, including the generation of atoms, nucleation, subsequent growth, secondary nucleation, and mesoscopic aggregation. (b) SEM images of a variety of surface topographies, types I−V, synthesized at various conditions (see text for details).

Our general protocol used to synthesize the Au sea urchin-like mesoparticles is based on the reduction of hydrogen tetrachloroaurate, $HAuCl_4$, by Fe suspension in aqueous solution (see Supporting Information). A scheme of the particle growth and topography of the products (together with the scanning electron microscopy (SEM) images) is illustrated in Figure 1b. In the metal nanocrystal synthesis according to the mechanism of LaMer and Dinegar,[29] after the start of the reaction (the first injection of the reductant in Figure 1) the concentration of Au atoms steadily increases with time as the precursor ($HAuCl_4$) is reduced. When the concentration reaches the point of supersaturation, the atoms start to aggregate into small clusters, i.e., nuclei, via self-(or homogeneous) nucleation. Once formed, these nuclei rapidly grow into nanocrystals of an increasingly larger size. Concurrently, the concentration of Au atoms in the solution decreases, until an equilibrium state is reached as determined by the chemical potential of the Au atoms in the solution and the chemical potential of the surface atoms of nanocrystals.[30] Besides growth via atomic addition, the nuclei and nanocrystals can directly coalesce into larger crystals via the particle-mediated aggregation process.[31,32] In fact, our previous studies on the synthesis of Ag mesocrystals[33] and crystal growth in gels[22] have indicated that high supersaturation and a high particle nucleation rate produce abundant small clusters, the building blocks for the mesostructures, and thus preferentially induce mesocrystal formation rather than the atom-mediated classical crystallization.[31]

DOI: 10.1021/nl103161q | *Nano Lett.* **2010,** *10,* 5006--5013

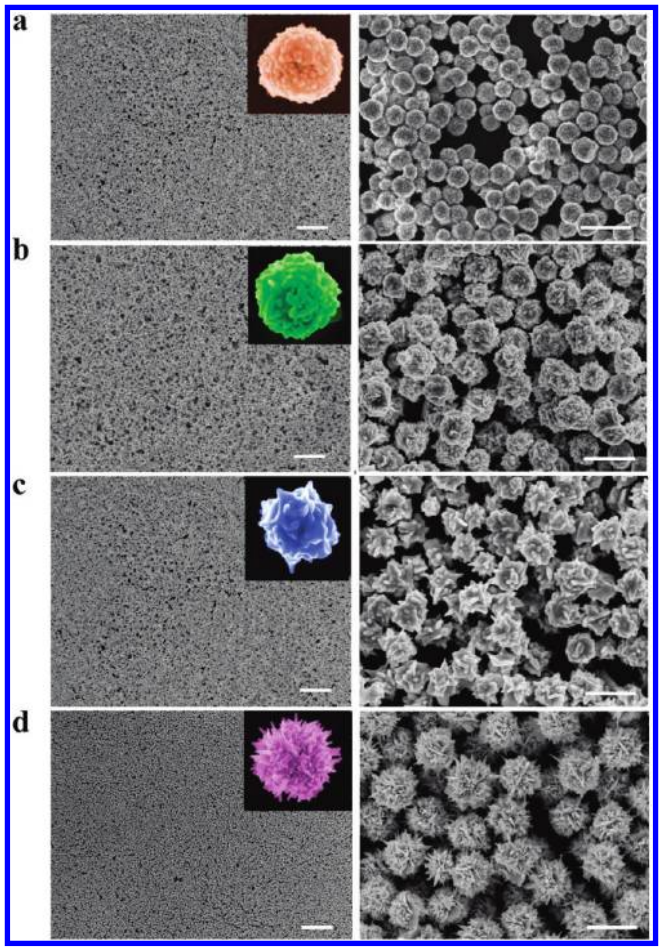

FIGURE 2. SEM images of different samples of gold mesoparticles self-assembled on a silicon wafer synthesized under different conditions: 20 mL of 10 mM $HAuCl_4$ (aqueous) reacts with 1 mL of Fe suspension and subsequently at different reaction times with various secondary Fe feeding amounts, (a) P1, (b) P2, (c) T1, (d) T2. The samples (a−d) with increasing surface texture correspond to the morphology types II, IV, III, and V, respectively (Figure 1). The scale bars on the left and right panels correspond to 20 and 1 μm, respectively.

In this study, analogous conditions of a high reduction and nucleation rate (a relatively high concentration of $HAuCl_4$) were also applied. Furthermore, during the growth of Au nanocrystals a secondary nucleation and growth process was initiated by a second injection of the reductant (Figure 1). This is similar to a procedure recently developed for preparing complex-shaped hierarchical crystals of ZnO and CdS.[34]

The consequence of our synthetic strategy is that the size and topography of Au mesoparticles can be widely tailored by controlling the amount and the time of the secondary injection of the Fe suspension as demonstrated in Figures 1 and 2. The degree of crystallinity and chemical composition of the Au mesoparticles were characterized using X-ray diffraction (XRD) and energy-dispersive X-ray spectroscopy (EDX) (Figures S3 and S4 in Supporting Information). Following the first injection of 1 mL of Fe suspension into 20 mL of 10 mM $HAuCl_4$ (aqueous), nearly spherical and relatively smooth Au primary particles of type I (i.e., sample P0 presented in Figures 1b and S5) with a particle size of about 400 nm were synthesized without the additional injection of the reductant. During the growth of Au nanocrystals, an atomic concentration fluctuation in the reaction solution can be created by quickly injecting a certain amount of Fe suspension again. This induces a secondary nucleation and growth process. When the conditions of this process are varied, the surface texture of the mesoparticles can be systematically developed. "Meatball" morphology, II and IV, is characteristic for moderate amounts of Fe suspension in the second injection. Furthermore, the surface texture can be somewhat increased from type II to type IV by delaying the second injection, e.g., from 5 to 10 min relative to the start of the reaction. As a consequence, the size of "meatball" particles increases from about 500 nm (sample P1 in Figure 2a) to about 600 nm (sample P2 in Figure 2b). A larger amount of Fe suspension in the second injection changes the product morphology to strongly textured types III (flower-like ribbed particles like sample T1 in Figure 2c) and V (sea urchin-like, spike-coated structures like sample T2 in Figure 2d)—depending on the time of the second injection (5 and 10 min, respectively). The number and density of the spikes on the particles of type V can be additionally enhanced by increasing the amount of Fe in the second injection, for example, from 0.7 to 2.0 mL as described in Methods (see Figures 2c,d and S6−S8). The size of the particles increases, correspondingly, from about 500 nm (Figure S6) to about 700 nm (Figure 2d). The highly textured sea urchin-like Au mesoparticles appear to comprise up to ∼200 tips having lengths of 50−100 nm and base thicknesses of 30−50 nm (Figure 2d). According to SEM and TEM images, the growth of all the above Au particle types must involve major contributions of mesoscopic aggregation probably in the early stage.[23,35] In contrast, if a very low initial concentration of $HAuCl_4$ (aqueous) is applied, e.g., 0.1 mM, smooth and faceted crystalline particles are produced like sample S0 presented in Figure S9 in Supporting Information. Under these conditions (low reduction and nucleation rate), Au particles likely grow near thermodynamic equilibrium via the "classical" atom-by-atom growth process.[22] Note that all of the different products described above demonstrate quite narrow distributions of size and morphology type (Figures 2 and S5−S9).

High-resolution transmission electron microscopy (HR-TEM) and selected area electron diffraction (SAED) provide further insight into the structure of Au mesoparticles. Figure 3a shows a typical bright-field TEM image of moderately textured mesoparticles from sample T1. It is clearly seen that these irregularly shaped particles are composed of many small nanoparticles with a size of ∼50 nm (the building blocks of the mesoscopic assembly) as further illustrated for two individual particles in panels b and d of Figure 3. The SAED pattern in Figure 3c indicates that the whole mesoparticle shown in Figure 3b is highly crystallographically

DOI: 10.1021/nl103161q | *Nano Lett.* **2010,** *10,* 5006–5013

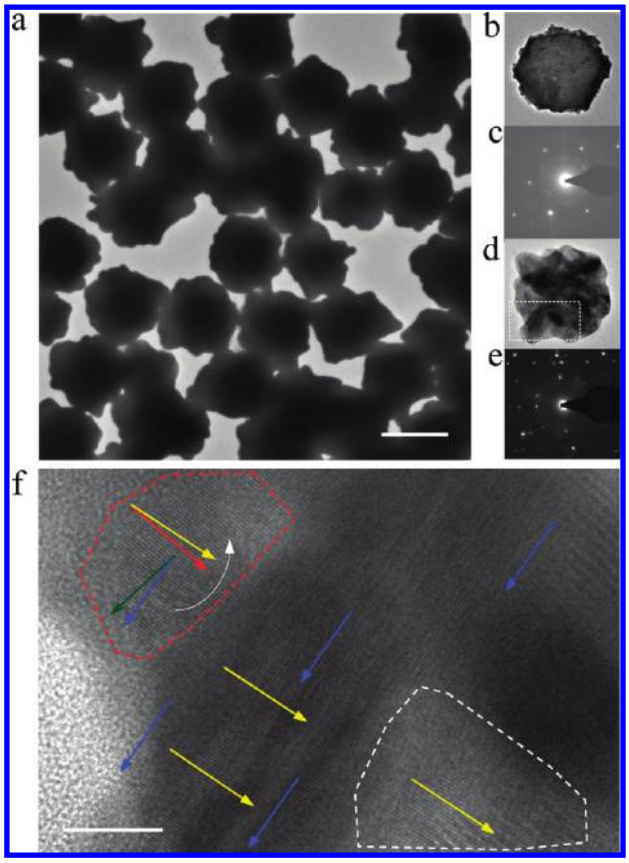

FIGURE 3. TEM images of gold mesoparticles for sample T1. (a) TEM image of Au mesoparticles. (b−e) TEM images and corresponding SAED patterns of individual particles. (f) HRTEM image obtained from the dashed box area in (d). Blue and yellow arrows indicate nanoparticle subunits with the same crystallographic orientation; green and red ones indicate a subunit with a small angle mismatch. The scale bars in (a) and (f) correspond to 500 and 5 nm, respectively.

aligned. A few isolated symmetrical spots in the diffraction pattern (Figure 3e) of the whole particle shown in Figure 3d suggest a common orientation with a small angle lattice mismatch between the nanoparticle building units. A magnified HRTEM image (Figure 3f) obtained from the box area of Figure 3d supports this suggestion. It shows three nanoparticles sharing the same crystallographic orientation in the junction regions and only one particle with a small angle mismatch (red dashed area in Figure 3f). This is a typical situation during the mesoscale transformation of mesoparticles, involving the oriented attachment[35] or grain rotation[36] of the building units. The existence of nanoscale protrusions or deep crevices between them can be clearly observed in the white contrastive area of the HRTEM image. When the multiple tips grow up via a secondary nucleation and growth process and then form the sea urchin-like Au mesoparticles, the structure, e.g., sample T2, displays a polycrystalline SAED pattern as shown in Figure S10c owing to the random orientation of such tips (Figure S10a,b in the Supporting Information). The individual tip demonstrates significant crystal defects (probably twins or stacking fault) along the axial direction of the single tip (Figure S10d and inset in the Supporting Information). We note that the distinctive mesostructures consisting of nanoparticle interfaces and sharp multitips can also be very useful in the exploitation of novel properties of Au mesoparticles, e.g., localized surface Plasmon resonances (LSPRs) and biosensors, because these rough surfaces can contribute to an enhanced reactivity.[37]

The SERS properties of individual Au mesoparticles and their dense arrays (see below) were evaluated by using crystal violet (CV) and *p*-mercaptoaniline (pMA) (Supporting Information), well-known SERS analytes. For measurements on individual mesoparticles, silicon wafers sparsely coated with mesoparticles were used. Figure 4a shows an optical microscopic image of such a sample with small aggregates of a few particles and single particles randomly distributed on the surface. An individual particle was visually identified within the laser spot. Figure 4b presents the typical SERS spectra of CV adsorbed on the individual Au mesoparticles P0, P1, T1, and T2, respectively, which were measured with a Raman microscope at 633 nm excitation, applying a low-magnification objective (~3 μm laser spot on the sample), 0.1 mW excitation power, and 20 s acquisition time. The SERS spectra reveal the characteristic peaks of CV, for instance, at 1172, 1371, and 1619 cm^{-1}, and correspond well to the ordinary Raman spectra of CV in the solid state and in aqueous solution. There is an apparent trend of increasing SERS signals with increasing surface texture: the average signals are found to scale as 81:30:8:1 for the particles T2, T1, P1, and P0, respectively. Quantification of the EFs is not trivial and subject to several assumptions as the number of adsorbed molecules is poorly defined and measured up to now. In this study, following the procedure and assumptions described in refs 38 and 39 for CV molecules and refs 41−43 for pMA molecules (see details in Supporting Information), we estimated EFs for both CV and pMA to be about ~10^6 and ~10^7 for the individual mesoparticles P1 and T2, respectively. It should be noted that these are the values "averaged" over a mesoparticle surface due to the relatively large laser excitation spot (~3 μm diameter) used. Correspondingly, EF at "hot spots" may significantly exceed the above values, if measured with a higher spatial resolution. The current estimation of the SERS EFs for various Au mesoparticles is consistent with ref 13 in which Wang estimated a value of EF ~10^6−10^7 for their Au "meatballs", which showed a quite similar morphology, size, and EF as our sample P1. Therefore, for sample T2, the estimated EF of ~10^7 is justifiable. Note that due to complex plasmonic patterns in relatively large and textured Au particles, even a single particle can potentially be an efficient single particle SERS (sp-SERS) "substrate" with multiple and bright "hot spots".

To corroborate the observed relationship between the SERS activity and surface topography of the Au mesoparticles, we have applied the discrete dipole approximation (DDA) method to calculate the local electric field intensity

DOI: 10.1021/nl103161q | *Nano Lett.* **2010,** *10,* 5006–5013

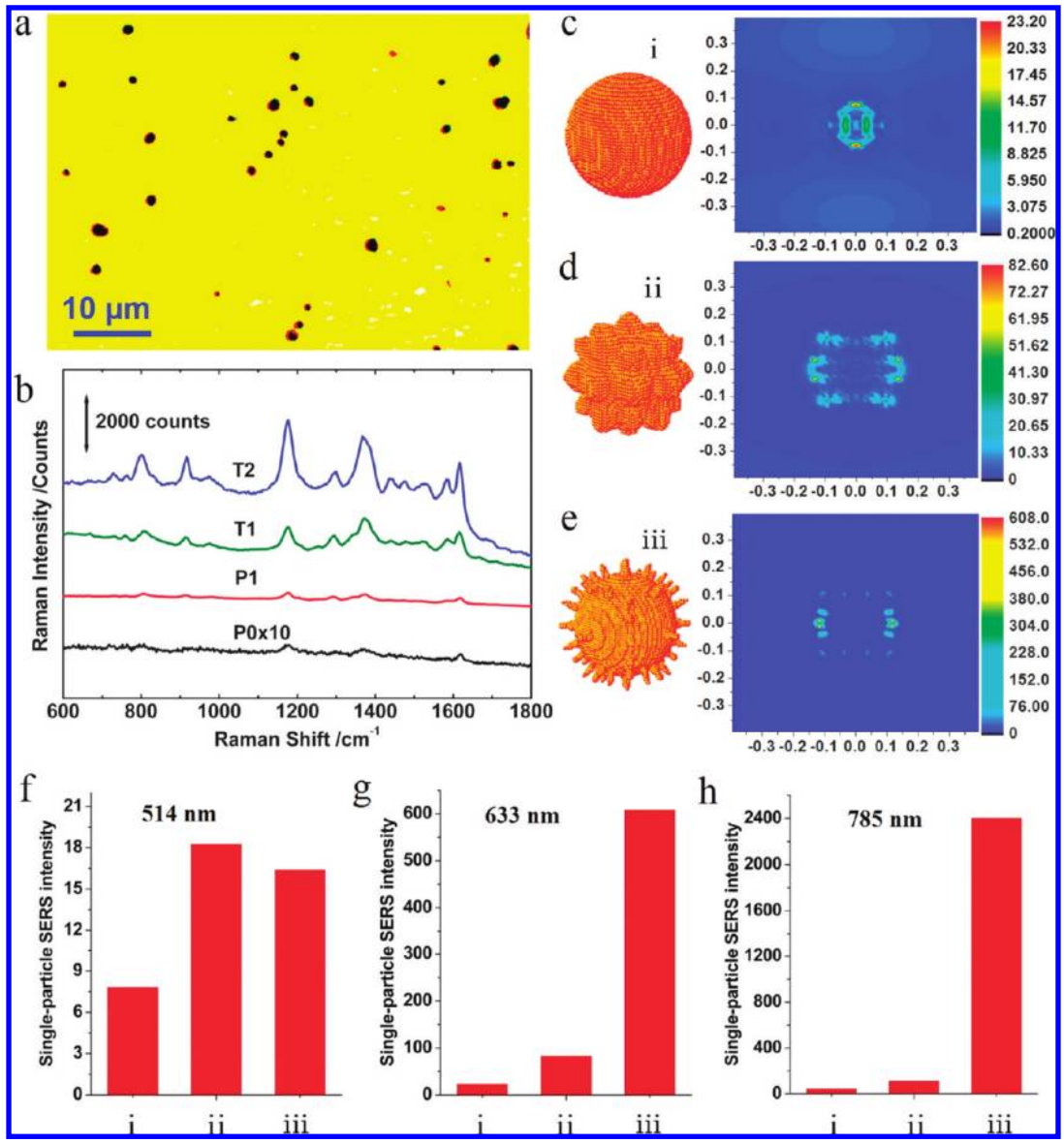

FIGURE 4. SERS spectra and E-field amplitude patterns of individual particles: (a) optical microscope image of a substrate with individual mesoparticles obtained from sample T2; (b) SERS spectra of crystal violet on individual particles with increasing surface texture, P0, P1, T1, and T2 (morphology types I, II, III and V, respectively, see Figure 1) and excitation at 633 nm; (c−e) model gold particles (i−iii) and corresponding calculated distributions of the local electric field intensity (color-coded relative $|E|^2$ values) across air-suspended particles irradiated from the top at 633 nm; (f−h) maximal electric field enhancements calculated for models (i−iii) at excitation wavelengths of 514, 633, and 785 nm, respectively.

around model Au particles irradiated with monochromatic light at 514, 633, and 785 nm (see details in Supporting Information). Three model particles were studied. They have the same external diameter of 400 nm but a different surface texture: (i) smooth, (ii) meatball, and (iii) sea urchin-like particles as shown in Figure 4c−e, or, in more detail, in Figure S11 (Supporting Information). The surface of (ii, iii) was textured with multiple half balls (50 nm diameter) and spikes (50 nm long and 20−30 nm thick), respectively. The surface topography of the models (i−iii) roughly simulates that of the Au mesoparticles of types I, II, and V, respectively (see Figure 1b). The right panels in Figure 4c−e show the typical distributions of the electric field strength E (plotted as color-coded $|E|^2$) calculated in a plane across a vertical axis of these model particles irradiated from above at 633 nm. As one might have anticipated, the most localized and enhanced electric field areas (compare the scale bars in Figure 4c−e) are found in the vicinity of spikes of the sea urchin model (iii). The maximal $|E|^2$ enhancement is found to be about 20, 80, and 600 for (i−iii), respectively. In other words, the sea urchin structure is clearly favored as the one potentially demonstrating the largest SERS enhancement (proportional to $\sim|E|^4$), in agreement with the experimental data (see above). It is well-known that the SERS effect can be optimized when the excitation light wavelength matches to the plasmonic resonance of the metal nanostructure.[44]

DOI: 10.1021/nl103161q | *Nano Lett.* **2010,** *10,* 5006–5013

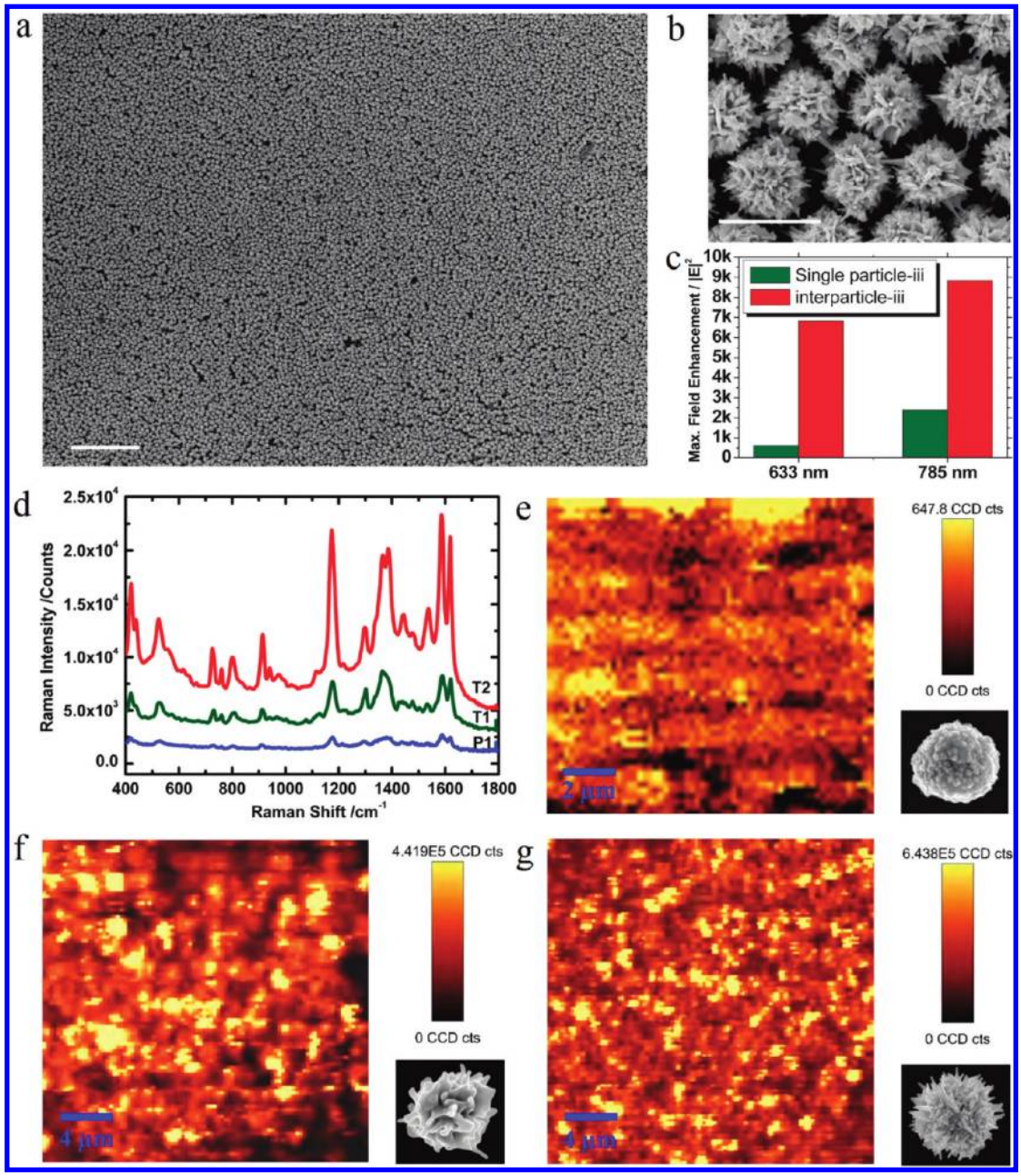

FIGURE 5. SEM images, SERS spectra, and SERS mapping for 2D arrays of gold mesoparticles: (a) SEM image of a dense monolayer array of sea urchin-like mesoparticles (sample T2) self-assembled on a silicon wafer; (b) magnified SEM image and (c) the maximum field enhancement for single particle and two interacting particles at various wavelengths from DDA calculations; (d) SERS spectra of crystal violet adsorbed on self-assembled arrays of samples P1 (blue), T1 (green), and T2 (red), obtained with 785 nm excitation; (e−g) Raman images of the arrays of sample P1, T1, and T2, respectively, displaying a color-coded area by mapping the CV Raman peak at ∼1172 cm^{-1}. The right bars of each image are the average CCD counts after subtracting background contributions. The scale bars shown in (a) and (b) correspond to 20 and 1 μm, respectively.

Our calculations indicate that the dependence of the SERS effect on the excitation wavelength may be especially strong for highly textured metal particles. This is illustrated by histograms of the maximal electric field ($|E|^2$) enhacement calculated for models (i−iii) irradiated at 514, 633, and 785 nm (Figure 4f−h). In fact, a relatively low and similar enhancement of ∼7−20 is predicted for all the model particles at 514 nm excitation. However, the difference between the models becomes very significant by red-shifting the excitation wavelength to 633 and 785 nm. Whereas the maximal electric field enhancement increases only moderately at these wavelengths for (i−ii), the value of (iii) increases dramatically up to ∼2400 at 785 nm (Figure 4f−h). Compared to the model (iii), the "real" sea urchin-like mesoparticles have an inhomogeneous surface texture and therefore likely exhibit broadened plasmonic resonances. Taking this into account, our calculations suggest that the optimal SERS excitation wavelength for these particles would

DOI: 10.1021/nl103161q | *Nano Lett.* **2010,** *10,* 5006−5013

lie in the red−near-infrared spectral region, particularly at 785 nm or larger. Although the excitation wavelength of 785 nm is not available for the investigation of sp-SERS in our experiment, these may be further supported by the UV−vis−NIR spectra as shown in Figure S12 (in the Supporting Information). As the surface topography changes to the more complex one, the localized surface plasmon bands appear in the red and infrared regions of the extinction spectrum.

Practical nanoparticle-based SERS substrates typically comprise an assembly (array) of these particles on a suitable support. As we have already mentioned, the homogeneity and stability of SERS signals over the whole area of such substrates are the other critical issues. In this regard, an important property of the mesoparticles synthesized in this work is that they can readily self-assemble on a surface. Specifically, we found that relatively dense mesoparticle arrays with a thickness between one and a few particles could be prepared by simply drop-casting a suspension of the mesoparticles in ethanol onto a silicon wafer and letting it dry under ambient conditions. Typical SEM images of such prepared arrays of different mesoparticle samples are collected in Figures 2 and S6−S9. Surprisingly, the best arrays in terms of close-packing and uniform thickness were obtained for sea urchin-like mesoparticles, in particular for sample T2. By adjusting drop-casting parameters (e.g., a concentration of the mesoparticles in ethanol suspension), quasi-hexagonally packed monolayer arrays over relatively large areas ($\sim mm^2$) could be obtained for sample T2 as illustrated in Figure 5a,b. Similar results were obtained by spin-coating a suspension of T2 onto a silicon wafer.

In accordance with their homogeneous assembly, the sea urchin-like mesoparticle arrays demonstrate uniform average SERS response. This was proven by taking the SERS spectra of CV at different locations in the array using a Raman spectrometer with the excitation wavelength of 785 nm, laser spot of $\sim 20\ \mu m$, and excitation power of 20 mW. Compared with the results measured at 633 nm for individual Au mesoparticles, the usage of a relatively larger laser spot (with a size of $\sim 20\ \mu m$) reveals more information, such as the interaction between Au mesoparticles. The Raman signals of CV measured in this way deviated for different T2 arrays (Figure 5a,b) by less than $\pm 5\%$, thus showing a good reproducibility. The typical SERS spectra obtained from samples P1, T1, and T2 at 785 nm excitation are compared in Figure 5d. The largest SERS response is again observed for the sea urchin-like particles—similar to the results for both the individual particles and arrays at 633 nm excitation. The homogeneity of the sea urchin-like T2 array is further supported by the SERS images of "hot spots" over self-assembled arrays. Figure 5e−g shows such images for P1, T1, and T2 arrays acquired with a lateral resolution of $\sim 0.5\ \mu m$ and presented as a color-coded integrated intensity of the characteristic peak of CV at 1172 cm^{-1}. The 3D projections of these images are also shown in Figure S13. It is clearly seen that the "hot spots" over the T2 array are the most uniform, abundant, and bright (compare the color-code intensity bars). According to the DDA calculations (Figure 5c) of the maximum field enhancement factor ($|E|^2$) for a single particle and two particle models at a 50 nm distance (Figure S14 and Table 1 in Supporting Information), the EF for the sea urchin-like mesoparticle array T2 exceeds the EF of the corresponding individual particles by $\sim 10-100$ times and thus can amount up to $\sim 10^8-10^9$. This can be explained by interparticle interactions in the array resulting in additional and/or more abundant "hot spots".[19,20,45,46] In fact, the Raman image obtained from specimen T2 demonstrates a comparable uniformity of the SERS signal (at ~ 200 nm resolution) relative to some SERS-active substrates produced by lithography techniques. It should be noted that, in lithography process, the empty space is around $\sim 1\ \mu m$ between nanostructural patterns where no Raman signals can be detected, e.g., in ref 47. However, in this study, the space between particles is around ~ 50 nm (Figure 5b). Within these spaces, some tips are very close and even touching. Therefore, the space can also contribute to the SERS signals.

In conclusion, a nanoparticle-mediated aggregation protocol has been exploited to generate high sensitive SERS substrates consisting of sea urchin-like Au mesoparticles. The surface topography of the Au mesoparticles can be accurately tailored from smooth spherical particles to highly textured sea urchin-like mesoparticles via a secondary nucleation and growth process. The sea urchin-like Au mesoparticles decorated with ~ 200 "spikes" are particularly interesting for SERS applications as they demonstrate high EFs up to 10^7 in magnitude for individual particles. Furthermore, these sea urchin-like mesoparticles can readily self-assemble into rather uniform and close-packed arrays on silicon wafers following a simple drop-casting deposition. The self-assembled monolayer arrays of the sea urchin-like Au mesoparticles demonstrate a uniform and reproducible SERS response. The EFs for such arrays can be increased by 1 or 2 orders of magnitude compared with the individual Au mesoparticles. These unique properties of the sea urchin-like Au mesoparticles appear to be very promising for applications as high-performance SERS substrates.

Acknowledgment. We thank Drs. Ralph Krupke, Babak Nasr, Di Wang, and Frank Schramm at Karlsruhe Institute of Technology (KIT), Institute of Nanotechnology, Germany, and Drs. Pedro Camargo, Benjamin Wiley, and Matthew Rycenga in Professor Younan Xia's group at Washington University, for their helpful discussions. J. X. Fang is grateful to the Alexander-von-Humboldt Foundation for a fellowship to support his stay in Germany. J. X. Fang was supported by the National Basic Research Program of China (no. 2010CB635101), the Fundamental Research Funds for the Central Universities (no. 08142008), and the National Natural Science Foundation of China (nos. 50901056 and 50834003). Z. Y. Li was supported

DOI: 10.1021/nl103161q | *Nano Lett.* **2010,** *10,* 5006--5013

by the National Natural Science Foundation of China under Grant Nos. 60736041 and 10874238.

Supporting Information Available. A description of our methods and materials, characterizations, additional figures, and additional references. This materials is available free of charge via the Internet at http://pubs.acs.org.

REFERENCES AND NOTES

(1) Li, J. F.; Huang, Y. F.; Ding, Y.; Yang, Z. L.; Li, S. B.; Zhou, X. S.; Fan, F. R.; Zhang, W.; Zhou, Z. Y.; Wu, D. Y.; Ren, B.; Wang, Z. L.; Tian, Z. Q. *Nature* **2010**, *464*, 392–395.

(2) Smythe, E. J.; Dickey, M. D.; Bao, J. M.; Whitesides, G. M.; Capasso, F. *Nano Lett.* **2009**, *9*, 1132–1138.

(3) Zhang, X.; Hicks, E. M.; Zhao, J.; Schatz, G. C.; , R. P.; Van, Duyne. *Nano Lett.* **2005**, *5*, 1503–1507.

(4) Technical information about Klarite: http://www.renishawdiagnostics.com.

(5) Kumbhar, A. S.; Kinnan, M. K.; Chumanov, G. *J. Am. Chem. Soc.* **2005**, *127*, 12444–12445.

(6) Fofang, N. T.; Park, T. H.; Neumann, Q.; Mirin, N. A.; Nordlander, P.; Halas, N. J. *Nano Lett.* **2008**, *8*, 3481–3487.

(7) Wei, A.; Kim, B.; Sadtler, B.; Tripp, S. L. *ChemPhysChem.* **2001**, *12*, 743–745.

(8) Garcia-Vidal, F. J.; Pendry, J. B. *Phys. Rev. Lett.* **1996**, *77*, 1163–1166.

(9) Wang, H.; Fu, K.; Drezek, R. A.; Halas, N. *J. Appl. Phys. B* **2006**, *84*, 191–195.

(10) Pecharroman, C.; Perez-Juste, J.; Mata-Osoro, G.; Liz-Marzan, L. M.; Mulvaney, P. *Phys. Rev. B* **2008**, *77*, No. 035418.

(11) Rodriguez-Fernandez, J.; Funston, A. M.; Perez-Juste, J.; Alvarez-Puebla, R. A.; Liz-Marzan, L. M.; Mulvaney, P. *Phys. Chem. Chem. Phys.* **2009**, *11*, 5909–5914.

(12) Bakr, O. M.; Wunsch, B. H.; Stellacci, F. *Chem. Mater.* **2006**, *18*, 3297–3301.

(13) Wang, H.; Halas, N. J. *Adv. Mater.* **2008**, *20*, 820–825.

(14) Liang, H. Y.; Li, Z. P.; Wang, W. Z.; Wu, Y. S.; Xu, H. X. *Adv. Mater.* **2009**, *21*, 4614–4618.

(15) Chen, J. Y.; Herricks, T.; Geissler, M.; Xia, Y. N. *J. Am. Chem. Soc.* **2004**, *126*, 10854–10855.

(16) Lee, E. P.; Chen, J. Y.; Yin, Y. D.; Campbell, C. T.; Xia, Y. N. *Adv. Mater.* **2006**, *18*, 3271–3274.

(17) Song, Y. J.; Yang, Y.; Medforth, C. J.; Pereira, E.; Singh, A. K.; Xu, H. F.; Jiang, Y. B.; Brinker, J.; Swol, F. v.; Shelnutt, J. A. *J. Am. Chem. Soc.* **2004**, *126*, 635–645.

(18) Nehl, C. L.; Liao, H. W.; Hafner, J. H. *Nano Lett.* **2006**, *6*, 683–688.

(19) Sau, T. K.; Murphy, C. J. *J. Am. Chem. Soc.* **2004**, *126*, 8648–8649.

(20) Xie, J. P.; Lee, J. Y.; Wang, D. I. C. *Chem. Mater.* **2007**, *19*, 2823–2830.

(21) Senapati, S.; Srivastava, S. K.; Singh, S. B.; Biswas, K. *Cryst. Growth Des.* **2010**, *10*, 4068–4075.

(22) Niederberger, M.; Cölfen, H. *Phys. Chem. Chem. Phys.* **2006**, *8*, 3271–3287.

(23) Fang, J. X.; Leufke, P. M.; Kruk, R.; Wang, D.; Scherer, T.; Hahn, H. *Nanotoday* **2010**, *5*, 175.

(24) Liang, X. D.; Gao, L.; Yang, S. W.; Sun, J. *Adv. Mater.* **2009**, *21*, 2068–2072.

(25) Liu, Z.; Wen, X. D.; Wu, X. L.; Gao, Y. J.; Chen, H. T.; Zhu, J.; Chu, P. K. *J. Am. Chem. Soc.* **2009**, *131*, 9405–9409.

(26) Fang, J. X.; Ma, X. N.; Cai, H. H.; Song, X. P.; Ding, B. J. *Nanotechology* **2006**, *17*, 5841–5845.

(27) Fang, J. X.; You, H. J.; Kong, P.; Yi, Y.; Song, X. P.; Ding, B. J. *Cryst. Growth Des.* **2007**, *7*, 864–868.

(28) Fang, J. X.; Ding, B. J.; Song, X. P.; Han, Y. *Appl. Phys. Lett.* **2008**, *92*, 173120–173122.

(29) LaMer, V. K.; Dinegar, R. H. *J. Am. Chem. Soc.* **1950**, *72*, 4847–4854.

(30) Peng, Z. A.; Peng, X. G. *J. Am. Chem. Soc.* **2002**, *124*, 3343–3353.

(31) Watzky, M. A.; Finke, R. G. *J. Am. Chem. Soc.* **1997**, *119*, 10382–10400.

(32) Kulak, A. N.; Iddon, P.; Li, Y.; Armes, S. P.; Cölfen, H.; Paris, O.; Wilson, R. M.; Meldrum, F. C. *J. Am. Chem. Soc.* **2007**, *129*, 3729–3734.

(33) Fang, J. X.; Ding, B. J.; Song, X. P. *Cryst. Growth Des.* **2008**, *8*, 3616–3622.

(34) Sounart, T. L.; Liu, J.; Voigt, J. A.; Huo, M.; Spoerke, E. D.; Mckenzie, B. *J. Am. Chem. Soc.* **2007**, *129*, 15786–15793.

(35) Penn, R. Lee.; Banfield, Jillian F. *Science* **1998**, *281*, 969–972.

(36) Herrmann, G.; Gleiter, H.; Baro, G. *Acta Metall.* **1976**, *24*, 353–359.

(37) Zhang, W. H.; Cui, X. D.; Yeo, B. S.; Schmid, T.; Hafner, C.; Zenobi, R. *Nano Lett.* **2007**, *7*, 1401–1405.

(38) Cai, W. B.; Ren, B.; Li, X. Q.; She, C. X.; Liu, F. M.; Cai, X. W.; Tian, Z. Q. *Surf. Sci.* **1998**, *406*, 9.

(39) Wang, Y.; Becker, M.; Wang, L.; Liu, J. Q.; Scholz, R.; Peng, J.; Gosele, U.; Christainsen, S.; Kim, D. H.; Steinhart, M. *Nano Lett.* **2009**, *9*, 2384–2389.

(40) Mohri, N.; Inoue, M.; Arai, Y. *Langmuir* **1995**, *11*, 1612–1616.

(41) Zhu, Z. H.; Zhu, T.; Liu, Z. F. *Nanotechnology* **2004**, *15*, 357–364.

(42) Jackson, J. B.; Halas, N. J. *Proc. Natl. Acad. Sci. U.S.A.* **2004**, *101* (52), 17930–17935.

(43) Gopinathm, A.; Boriskina, S. V.; Premasiri, W. R.; Ziegler, L.; Reinhard, B. M.; Nego, L. D. *Nano Lett.* **2009**, *9*, 3922–3929.

(44) Mulvihill, M.; Ling, X. Y.; Henzie, J.; Yang, P. D. *J. Am. Chem. Soc.* **2010**, *132*, 268–274.

(45) Xu, H. X.; Aizpurua, J.; Kall, M.; Apell, P. *Phys. Rev. E* **2000**, *62*, 4318–4324.

(46) Xu, H. X.; Bjerneld, E. J.; Kall, M.; Borjesson, L. *Phys. Rev. Lett.* **1999**, *83*, 4357–4360.

(47) Im, H.; Bantz, K. C.; Lindquist, N. C.; Haynes, C. L.; Oh, S. H. *Nano Lett.* **2010**, *10*, 2231–2236.

DOI: 10.1021/nl103161q | *Nano Lett.* **2010,** *10,* 5006–5013